Cyclodextrin-Functionalized Fe_3O_4@TiO_2: Reusable, Magnetic Nanoparticles for Photocatalytic Degradation of Endocrine-Disrupting Chemicals in Water Supplies

Rajesh Chalasani and Sukumaran Vasudevan*

Department of Inorganic and Physical Chemistry, Indian Institute of Science, Bangalore 560012, India

ABSTRACT Water-dispersible, photocatalytic Fe_3O_4@TiO_2 core–shell magnetic nanoparticles have been prepared by anchoring cyclodextrin cavities to the TiO_2 shell, and their ability to capture and photocatalytically destroy endocrine-disrupting chemicals, bisphenol A and dibutyl phthalate, present in water, has been demonstrated. The functionalized nanoparticles can be magnetically separated from the dispersion after photocatalysis and hence reused. Each component of the cyclodextrin-functionalized Fe_3O_4@TiO_2 core–shell nanoparticle has a crucial role in its functioning. The tethered cyclodextrins are responsible for the aqueous dispersibility of the nanoparticles and their hydrophobic cavities for the capture of the organic pollutants that may be present in water samples. The amorphous TiO_2 shell is the photocatalyst for the degradation and mineralization of the organics, bisphenol A and dibutyl phthalate, under UV illumination, and the magnetism associated with the 9 nm crystalline Fe_3O_4 core allows for the magnetic separation from the dispersion once photocatalytic degradation is complete. An attractive feature of these "capture and destroy" nanomaterials is that they may be completely removed from the dispersion and reused with little or no loss of catalytic activity.

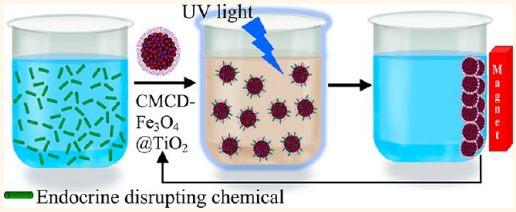

KEYWORDS: β-cyclodextrin · Fe_3O_4@TiO_2 core–shell nanocrystals · endocrine-disrupting chemicals · photocatalytic degradation · magnetic separation

Photoinduced redox chemical reaction occurring on irradiated semiconductor surfaces is a promising environmental remediation technology, especially for water-borne pollutants.[1] The advantages of this technique over traditional wastewater treatment methods include complete mineralization and high degradation efficiency in treating organic compounds at low concentrations.[2] One of the most popular and widely investigated photocatalysts for environmental applications is TiO_2 because of its chemical inertness, strong oxidizing power, cost effectiveness, and long-term stability against photo- and chemical corrosion.[3−5] The photoexcitation of TiO_2 induces electron–hole pair formation, and subsequent charge separation/migration/transfer leads to the production of highly reactive oxygen species such as OH radicals and superoxide on the surface of TiO_2 that can oxidize aquatic organic pollutants.[5,6] Typically, a photocatalytic reaction is conducted in a suspension of TiO_2 catalyst particles, either at the nano- or microscale. Although photocatalysis is efficient, the separation of the TiO_2 particles is a major bottleneck that limits the application of these photocatalytic processes for treating wastewaters.[7] Separation is important not just from a reusability perspective but also to avoid the adverse biological effects of the semiconductor nanoparticles even in the absence of light. A viable solution is to combine the photocatalytic activity of TiO_2 with the magnetism associated with iron oxide nanocrystals that are easily separable under modest magnetic fields. A similar strategy of combining the magnetic properties of magnetite particles and the affinity of TiO_2 toward phosphopeptides has been reported for the enrichment of phosphopeptides from

* Address correspondence to svipc@ipc.iisc.ernet.in.

Received for review January 19, 2013 and accepted April 21, 2013.

Published online April 21, 2013
10.1021/nn400287k

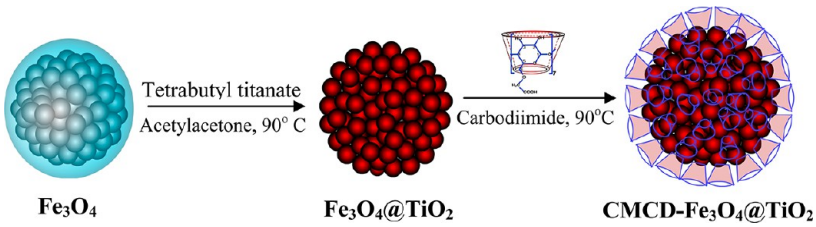

Scheme 1

complex mixtures.[8,9] The use of photocatalytic, magnetic TiO_2 submicrometer particles has also been explored.[10,11] Magnetic separation is a convenient approach for removing and recycling magnetic particles/composites, and the process has been used for removing As and organic pollutants from water.[12,13]

Some of the more hazardous chemical substances found in water supplies today are the endocrine-disrupting chemicals (EDC), bisphenol A (BPA) and phthalic acid esters that exhibit biological behavior similar to that of natural and synthetic estrogens with steroidal structures.[14,15] Both have been implicated in reproductive and sexual abnormalities in humans as well as wild life. They, however, continue to be used as they are important chemicals widely used in the plastic industry. BPA is used as the monomer for the production of polycarbonate plastics and is a major component of epoxy resins. Phthalates or phthalic acid esters (PAEs) are used as plasticizers for polyvinyl chloride (PVC) resins, cellulose film coatings, styrene, adhesives, cosmetics, as well as in pulp and paper manufacturing. Release of these chemicals into the ecosystem or wastewater effluent occurs during the production phase and *via* leaching and volatilization from plastic products during their usage and/or after disposal. There is an urgent need to develop methods to remove these EDCs from water supplies. Conventional methods that include biodegradation as well as absorption of the EDCs on suitable substrates suffer from the drawback that they require long times, making them unsuitable for effective wastewater treatment.[16] One of the more promising approaches is the use of TiO_2 for the photocatalytic degradation of EDCs.[17] The photodegradation of BPA and PAE by TiO_2 nanostructures has been demonstrated,[18−20] but it is unlikely that application based on these processes would be viable for reasons mentioned earlier, such as the difficulty of separation and hence reuse of the TiO_2 nanoparticles.

In an earlier report, we had showed how water-dispersible magnetite nanoparticles prepared by anchoring β-cyclodextrin cavities to the surface of 10 nm spherical magnetic nanoparticles can be used to remove both organic pollutants and arsenic from water in a single-step magnetic separation process.[13] The method exploited the hydrophobic cavity of the tethered cyclodextrins to capture nonpolar organic molecules present in water and the affinity of As ions toward iron to adsorb them on the magnetite nanocrystals. The magnetization of the spherical nanocrystals saturates at low magnetic fields (0.4 T) with appreciable magnitude (40 emu/g), and hence the particles are easily separated from aqueous dispersions. The magnetic nanoparticles along with the anchored CD cavities carrying their toxic cargo may then be removed from the aqueous media by application of modest magnetic fields (<0.5 T). Although the procedure was successful in removing organic contaminants from water, a serious limitation of the method is that it does not provide a route or strategy for the disposal of the toxic contaminants. This is a serious issue especially with EDCs and other persistent organic pollutants. Here we report the synthesis of a water-dispersible β-cyclodextrin-functionalized Fe_3O_4@TiO_2 core−shell nanoparticle that can both capture and photocatalytically destroy the organic EDCs present in water. The functionalized nanoparticles can be magnetically separated from the dispersion after photocatalysis and hence reused. Each component of the cyclodextrin-functionalized Fe_3O_4@TiO_2 core−shell nanoparticle has a crucial role in its functioning. The tethered cyclodextrins are responsible for the aqueous dispersibility of the nanoparticles and their hydrophobic cavities for the capture of the organic pollutants that may be present in water samples. The TiO_2 shell is the photocatalyst for the degradation and mineralization of the organics under UV illumination, and the magnetism associated with the Fe_3O_4 core allows for the magnetic separation from the dispersion once photocatalytic degradation is complete. Here we characterize the cyclodextrin-functionalized Fe_3O_4@TiO_2 core−shell nanoparticles by X-ray diffraction, electron microscopy, and magnetic measurements and demonstrate their application for the destruction of the EDCs, bisphenol A and dibutyl phthalate, on UV irradiation.

RESULTS AND DISCUSSION

Synthesis and Characterization of β-Cyclodextrin−Fe_3O_4@TiO_2. *Synthesis.* Cyclodextrin-capped Fe_3O_4@TiO_2 nanoparticles were prepared by a two-step procedure (Scheme 1). In the first step, monodisperse, water-dispersible Fe_3O_4 nanocrystals that form the core were coated with a TiO_2 shell. The water-dispersible Fe_3O_4 nanocrystals were prepared by an earlier reported procedure.[13] Fe_3O_4 nanocrystals

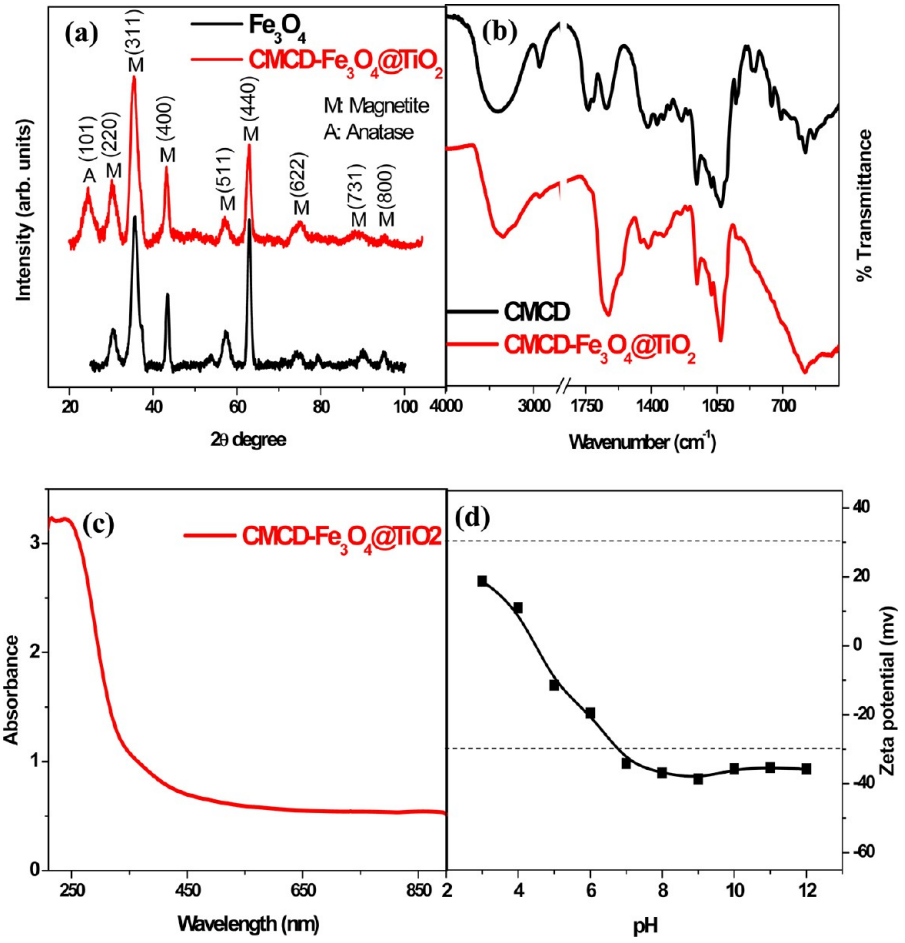

Figure 1. (a) XRD pattern of CMCD-Fe_3O_4@TiO_2. For comparison, the diffraction pattern of Fe_3O_4 is shown. (b) FTIR spectra of CMCD-Fe_3O_4@TiO_2 and β-CMCD. (c) UV−visible spectra of an aqueous dispersion of CMCD-Fe_3O_4@TiO_2. (d) Zeta-potential of aqueous dispersions of CMCD-Fe_3O_4@TiO_2 at different pH values.

were obtained from the thermal decomposition of FeOOH in a high boiling solvent, octadecene.[21] This procedure is known to give spherical monodisperse Fe_3O_4 nanocrystals. The TiO_2 shell was prepared by the hydrolysis of tetrabutyl titanate (TBT) in an ethanol/water mixture in the presence of the water-dispersible Fe_3O_4 nanocrystals.[8,9] To obtain a uniform shell, the rate of hydrolysis of TBT has to be controlled. This was done by addition of acetylacetone which is known to form a stable chelate complex with TBT whose rate of hydrolyses at 90 °C is slow.[22,23] The as-prepared Fe_3O_4@TiO_2 nanoparticles were removed from the suspension by magnetic separation, and their surface was modified by capping with carboxymethyl−β-cyclodextrin (CMCD) cavities. This was achieved by treating Fe_3O_4@TiO_2 nanoparticles with CMCD in water in the presence of carbodiimide at 90 °C. The carboxylic groups of CMCD react with carbodiimide to form an intermediate that subsequently reacts with the surface hydroxyl groups of TiO_2 to form metal carboxylates.[24]

The CMCD-functionalized Fe_3O_4@TiO_2 (CMCD-Fe_3O_4@TiO_2) was magnetically separated from the dispersion and washed to remove excess CMCD. Thermogravimetric and elemental analysis indicated that there were 0.101 mols of CMCD per gram of the CMCD-Fe_3O_4@TiO_2 (see Supporting Information). The surface-modified CMCD-Fe_3O_4@TiO_2 nanocrystals are easily dispersed in water. It was difficult to ascertain the maximum amount that can be dispersed as above a concentration of 20 mg/mL the dispersion turns viscous and opaque.

Characterization. X-ray Diffraction (XRD). The XRD patterns of CMCD-Fe_3O_4@TiO_2 nanoparticles and Fe_3O_4 (magnetite) nanocrystals are shown in Figure 1a. The patterns are similar; the Bragg reflections of CMCD-Fe_3O_4@TiO_2 appearing at the same position as that of the Fe_3O_4 nanocrystals. The CMCD-Fe_3O_4@TiO_2, however, shows an additional broad peak at a Bragg angle corresponding to a spacing of 3.25 Å; this may be assigned to the 101 reflection of a poorly crystalline TiO_2 anatase phase. X-ray photoelectron spectra of the CMCD-Fe_3O_4@TiO_2 nanoparticles show Ti in the +4 oxidation state. The spectrum in the Ti 2p region is quite similar to that of crystalline TiO_2 (see Supporting Information). It may be noted that the crystalline TiO_2 phases, anatase, rutile, and brookite, are high-temperature phases.[25,26] The procedure followed here

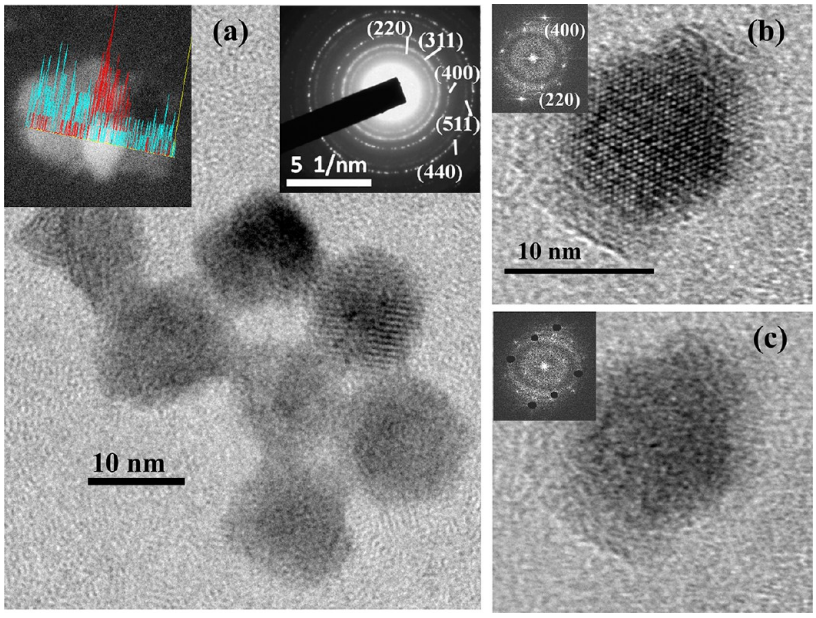

Figure 2. (a) TEM images of the CMCD-Fe_3O_4@TiO_2 nanocrystals. The inset on the left shows the STEM-HAADF image along with elemental mapping based on EDS. The signal in blue corresponds to Ti and that in red to Fe. The inset on the right is the selected area electron diffraction pattern. (b) HRTEM image of a single particle of CMCD-Fe_3O_4@TiO_2 along with the FFT generated diffraction pattern. (c) Image reconstructed by an inverse FFT of the diffraction pattern after masking the diffraction spots of Fe_3O_4.

to prepare Fe_3O_4@TiO_2 nanocrystals follows a low-temperature, soft-chemical route that is unlikely to result in the formation of crystalline TiO_2.

Infrared Spectroscopy. The capping of the Fe_3O_4@TiO_2 nanoparticles by CMCD was confirmed by the presence of peaks due to β-cyclodextrin in the infrared spectrum (Figure 1b). The band at 2929 cm^{-1} is due to the C−H stretch of cyclodextrin, and the bands at 1157 and 1029 cm^{-1} are due to the C−O stretch and the antisymmetric glycosidic (C−O−C) vibrational modes. The band at 1735 cm^{-1} due to the carbonyl stretch of the carboxylic acid in CMCD is absent in the spectra of CMCD-Fe_3O_4@TiO_2, instead two new bands at 1558 and 1418 cm^{-1} appear that may be assigned to the asymmetric and symmetric carboxylate stretching modes, respectively. The broad band between 400 and 700 cm^{-1} seen in the spectrum of CMCD-Fe_3O_4@TiO_2 may be assigned to the Ti−O−Ti stretching modes. The infrared spectra confirm the modification of the Fe_3O_4@TiO_2 by cyclodextrin cavities that are tethered to the surface by a carboxylate linkage. It is the exposed hydroxyl groups located at the rim of the anchored cyclodextrin cavities that render the surface of the CMCD-Fe_3O_4@TiO_2 nanoparticles hydrophilic and ensure their aqueous dispersibility.

Optical Spectra. The UV−visible spectrum of an aqueous dispersion of the CMCD-Fe_3O_4@TiO_2 nanoparticles is shown in Figure 1c. It shows an absorption onset below 360 nm (3.44 eV). The band gap of bulk TiO_2 is 3.2 eV.[27] The blue shift could be due to a combination of factors, particle size, surface groups, or the presence of Fe as a dopant.

Zeta-Potential. The zeta-potential (ζ) of aqueous dispersions of CMCD-Fe_3O_4@TiO_2 at different values of pH is shown in Figure 1d. The zeta-potential is an important factor for characterizing the stability of colloidal dispersions and provides a measure of the magnitude and sign of the effective surface charge associated with the double layer around the colloid particle. Generally, particles with zeta-potentials more positive than +30 mV or more negative than −30 mV are considered to form stable dispersions due to interparticle electrostatic repulsion.[28] It may seen that ζ of the CMCD-Fe_3O_4@TiO_2 dispersion drops below −30 mV only above a pH value of 7. The fact that CMCD-Fe_3O_4@TiO_2 forms stable dispersions below this pH value indicates that a mechanism different from electrostatic repulsion must be responsible for the stability of the dispersion in the pH range of 3 to 7. In this pH range, it is the hydrophilicity associated with the hydroxyl groups present on the rims of the tethered cyclodextrin cavities that play a major role in stabilizing the dispersion. Above pH 7, ionization of residual carboxylic groups and the cyclodextrin hydroxyls results in the negative charge buildup on the particles and the dispersions are stabilized primarily by electrostatic repulsion .

Transmission Electron Microscopy (TEM). The TEM images of the CMCD-functionalized Fe_3O_4@TiO_2 nanocrystals are shown in Figure 2. The images were recorded after spotting the grid with an aqueous dispersion of the nanocrystals. The images show that the nanocrystals have an average diameter of 12 nm and appear to have a darker inner core of around 9 nm.

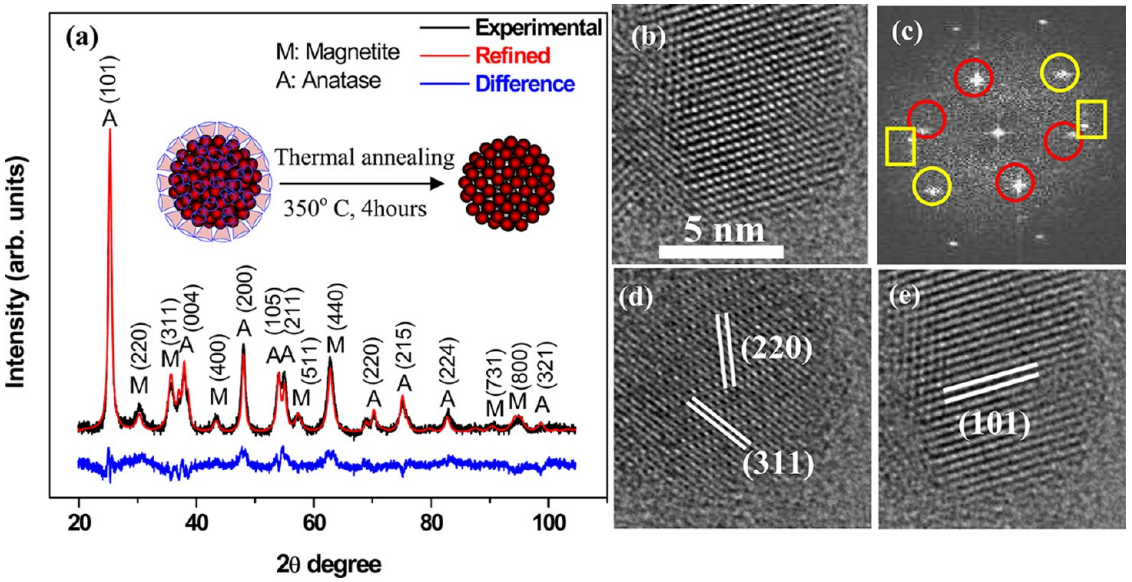

Figure 3. (a) X-ray diffraction patterns of the thermally annealed Fe_3O_4@TiO_2 nanocrystals along with the Rietveld refinement fits obtained by considering the presence of a mixture of magnetite (Fe_3O_4) and anatase (TiO_2). (b) HRTEM image of the Fe_3O_4@TiO_2 nanocrystal. (c) Diffraction pattern generated by a FFT of the image. The red circles are the 101 spots of TiO_2. The yellow rectangles and circles are the 220 and 311 spots of Fe_3O_4. (d) Image reconstructed by an inverse FFT after masking the 101 spots of TiO_2 (red circles). (e) Image reconstructed by an inverse FFT after masking the 220 (yellow rectangle) and 311 (yellow circle) spots of Fe_3O_4.

Scanning transmission electron microscopy high-angle annular dark-field (STEM-HAADF) imaging is a useful method for characterizing core−shell particles with close atomic numbers. In this method, the signal is directly proportional to the thickness and atomic number of the specimen. The STEM-HAADF image of the CMCD-Fe_3O_4@TiO_2 (left inset of Figure 2a) shows a bright core region probably corresponding to the iron oxide. An elemental mapping based on energy-dispersive X-ray spectroscopy (EDS) is shown in left inset of Figure 2a. The figure shows the line scanning profile based on EDS, superimposed on the STEM-HAADF image. The signal in blue corresponds to Ti and the signal in red to Fe. It may be seen that the blue signal is distributed uniformly throughout the particle, while the red signal is concentrated mainly at the center of the particle. The EDS profiles confirm a core−shell structure for the CMCD-Fe_3O_4@TiO_2 nanocrystals with the iron oxide forming the core. In order to identify the phases of the oxide present, the selective area electron diffraction pattern was examined. The pattern shows rings that may be indexed to the 220, 311, 400, 511, and 440 planes of Fe_3O_4 (JCPDS File No. 19-0629). Diffraction from the TiO_2 phase was not observed, indicating that the TiO_2 shell is amorphous. This is in agreement with the X-ray diffraction data (Figure 1a) where only Bragg diffractions corresponding to Fe_3O_4 were observed.

To reconfirm these observations, the HRTEM image of a single CMCD-Fe_3O_4@TiO_2 nanoparticle and its corresponding fast Fourier transform (FFT) generated diffraction pattern was examined (Figure 2b). The FFT diffraction pattern (inset of Figure 2b) shows two different types of spots that may be indexed to the 220 and 400 planes of magnetite. These spots were then masked and the image reconstructed by an inverse FFT. The reconstructed image is of almost uniform brightness and does not show any lattice fringes, confirming that the particle consists of a crystalline core and an amorphous shell and in conjunction with the elemental mapping can be identified as Fe_3O_4 and TiO_2, respectively.

Thermally Annealed Fe_3O_4@TiO_2. In order to identify the TiO_2 phase, which in the as-prepared CMCD-Fe_3O_4@TiO_2 exists as an amorphous shell, the nanocrystals were thermally annealed in air at 350 °C for 4 h. During annealing, the TiO_2 phase crystallizes, but at these temperatures, the anchored cyclodextrin cavities undergo thermal decomposition and the material is no longer dispersible in water. The X-ray diffraction patterns of the annealed Fe_3O_4@TiO_2 are shown in Figure 3a. The pattern shows additional reflections not seen in the XRD pattern of the as-prepared CMCD-Fe_3O_4@TiO_2 that may be assigned to a crystalline TiO_2 phase. Quantitative analysis of the XRD data was undertaken with a full pattern fitting procedure based on the Rietveld method using the program FULLPROF.[29] The Rietveld refinement was performed assuming that two crystalline phases were present, Fe_3O_4 and TiO_2. The lattice parameters and atomic coordinates of magnetite along with either the anatase or rutile or brookite phases of crystalline TiO_2 were used in the refinement. The best agreement with experimental data was obtained using the lattice parameters and atomic coordinates of anatase (Figure 3a; details of the refinement procedure are provided as part of the

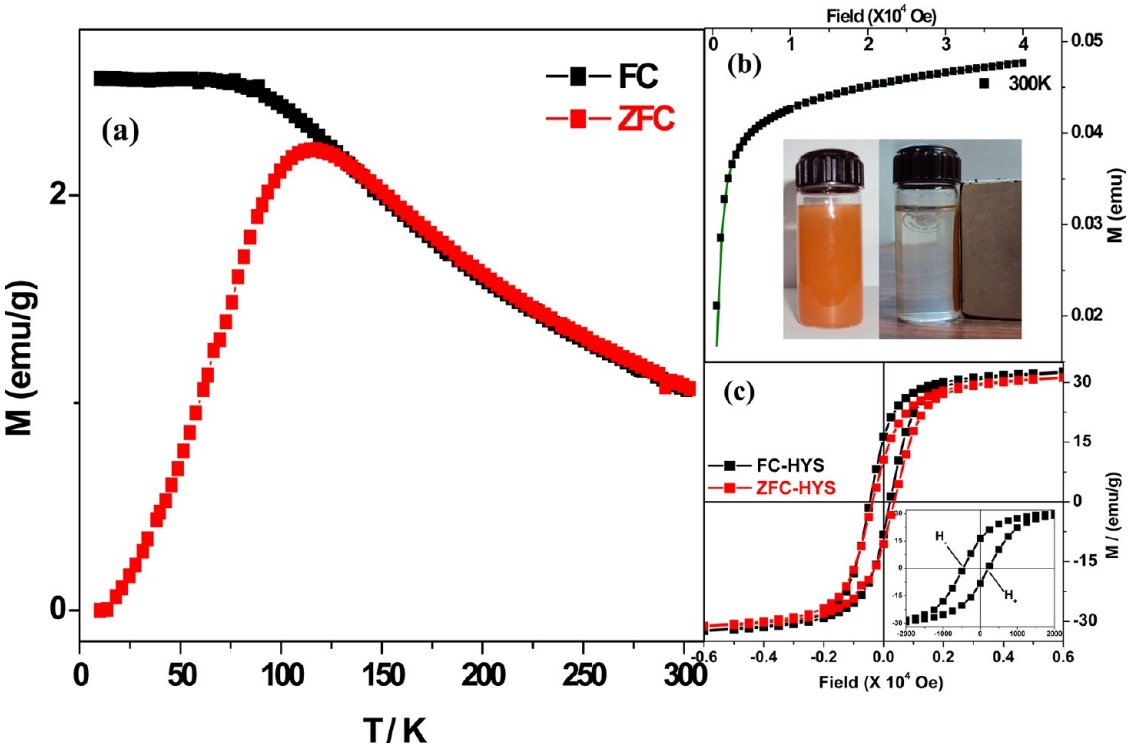

Figure 4. (a) Temperature dependence of the zero-field-cooled (ZFC) and field-cooled (FC) magnetic moment of the CMCD-Fe_3O_4@TiO_2 nanocrystals. (b) Isothermal magnetization curves for CMCD-Fe_3O_4@TiO_2 nanocrystals above their blocking temperature (300 K). The solid line is fit to the modified Langevin expression (eq 1) for a superparamagnet. The inset shows magnetic separation of the CMCD-Fe_3O_4@TiO_2 nanoparticles from their aqueous dispersion. (c) Hysteresis loops recorded at 10 K following FC and ZFC procedures. The inset shows an expanded view of the FC loop with the intersections on the field axis indicated.

Supporting Information). The weight percentages of magnetite and anatase that gave the best fit were 73 and 27%, respectively.

The annealed Fe_3O_4@TiO_2 nanoparticles were also examined by electron microscopy. The HRTEM images and the FFT generated diffraction spots are shown in Figure 3b,c. In the FFT generated diffraction pattern, two sets of spots may be indexed, based on their *d*-spacing, as the (220) and (311) of magnetite (JCPDS File No. 19-0629). The remaining spots are indexed to the (101) plane of anatase (JCPDS File No. 21-1272). In an attempt to locate the magnetite and anatase phases in the particle, the spots corresponding to these phases were separately masked and the corresponding image reconstructed by an inverse FFT. The reconstructed image obtained after masking the 101 spots of anatase is shown in Figure 3d. Two different lattice fringes corresponding to 220 and 311 planes of magnetite can be seen. In the second step, the 220 and 311 spots corresponding to magnetite were masked, and the image was reconstructed (Figure 3e). The image shows lattice fringes corresponding to the 101 planes of anatase. The analysis indicates that both Fe_3O_4 and TiO_2 exist together with a core−shell structure in the particle.

Magnetic Properties. The temperature dependence of the magnetic moment, *M* (*T*), of the CMCD-Fe_3O_4@TiO_2 nanocrystals, in an applied magnetic field (0.01 T), was measured after field cooling (FC) and after zero-field cooling (ZFC) from 300 to 10 K (Figure 4a). The blocking temperature, T_B, is the temperature at which superparamagnetism sets in and may be identified as the temperature below which the FC and ZFC magnetization curves diverge. Above T_B, the remanence and coercivity of the particles vanish due to thermal averaging and the curves coincide. For the CMCD-Fe_3O_4@TiO_2 nanocrystals, $T_B \approx 115$ K, and above this temperature, the nanocrystals are superparamagnetic. This was confirmed by fitting the isothermal magnetization as a function of field at temperatures above the blocking temperature to a modified Langevin function.

$$M = M_0 L(x) + \chi H \quad (1)$$

where $L(x) = [\coth(x) - (1/x)]$ is the Langevin function, M_0 is the saturation magnetization, $x = \mu_p H/k_B T$, where μ_p is the particle magnetic moment, k_B the Boltzmann constant, and χ the susceptibility of the ferromagnetic nanoparticles as predicted by Neel for particles with antiferromagnetic interactions.[30] The saturation magnetization value of CMCD-Fe_3O_4@TiO_2 at 300 K is 28 emu/g.

The origin of the comparatively high blocking temperature[31] and saturation magnetization values of the CMCD-Fe_3O_4@TiO_2 nanoparticles may be understood from the FC and ZFC magnetization hysteresis

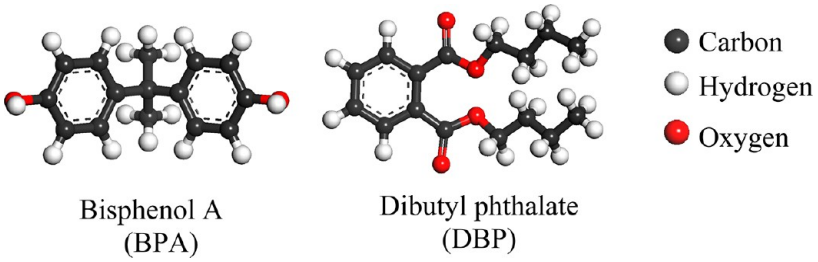

Scheme 2

loops recorded at 10 K (Figure 4c). A comparison of the loops shows that the FC hysteresis is broadened and exhibits a coercivity enhancement, revealing induced uniaxial or multiaxial anisotropy. There is a negative shift from the origin along the field axis after field cooling. A similar behavior had been observed for the iron oxide nanocrystals prepared by the procedures used here, such as thermal decomposition of FeOOH in a high boiling solvent, and had been ascribed to exchange bias due to trace amounts of the antiferromagnet FeO present. A hysteresis loop shift is commonly observed when a ferromagnet is in contact with an antiferromagnet and is a manifestation of exchange bias.[32] Magnetic exchange coupling induced at the interface between the ferromagnetic and antiferromagnet can provide an extra source of anisotropy leading to magnetization stability. In nanoparticles, the presence of an exchange bias field leads to higher blocking temperatures, T_B, and coercive fields, H_c, as compared to particles where such fields are absent.[33] The exchange bias field, H_e, is defined as the offset of the hysteresis loop along the field axis $H_e = -(H_+ + H_-)/2$, where H_+ and H_- are the intersections on the field axis at increasing and decreasing fields in the FC hysteresis loop and the coercive field, H_c, as half its width ($H_c = (H_+ - H_-)/2$). The values of H_e and H_c for the CMCD-Fe_3O_4@TiO_2 nanoparticles are 10 and 34 mT, respectively.

The CMCD-Fe_3O_4@TiO_2 nanoparticles are easily dispersed in water, forming an orange colored dispersion at low concentrations and a darker viscous fluid at higher concentrations. The dispersions are stable and cannot be separated by ultracentrifugation at speeds up to 12 000 rpm. The dispersibility may be attributed to the exposed hydroxyl groups located on the rims of the cyclodextrin cavities. At the same time, the Fe_3O_4 core ensures that the magnetization values are sufficiently high for the nanocrystals to be easily separated from their aqueous dispersions by application of modest magnetic fields (<0.4 T) using a small permanent magnet (inset of Figure 4b). Typically, separation was effected within 2−3 min in the presence of the magnet.

In summary, we have shown that the CMCD-Fe_3O_4@TiO_2 nanoparticles have a core−shell structure; Fe_3O_4 forms the crystalline core while TiO_2 forms an amorphous shell. The surface of the TiO_2 shell has been functionalized by anchoring CMCD cavities. The hydroxyl groups present at the rim of the cyclodextrin cavities render the surface of the CMCD-Fe_3O_4@TiO_2 nanoparticles hydrophilic. The particles are easily dispersed in water, but the presence of the magnetic iron oxide core ensures that they are easily separated from aqueous dispersions on application of modest magnetic fields. Of particular significance to the present study is the fact that the integrity of the anchored cyclodextrin is preserved and its hydrophobic cavity is available for the inclusion of organic guest molecules.

Photocatalytic Degradation Using CMCD-Fe_3O_4@TiO_2. In this section, we report the photocatalytic degradation of the endocrine-disrupting chemicals, bisphenol A (BPA) and the phthalic acid ester, dibutyl phthalate (DBP) (Scheme 2), in water using the water-dispersible CMCD-Fe_3O_4@TiO_2.

Adsorption Measurements. The adsorption of BPA and DBP by the CMCD-Fe_3O_4@TiO_2 from their aqueous solutions was studied in the batch mode. The sorption isotherms were measured by equilibrating aqueous dispersion of the CMCD-Fe_3O_4@TiO_2 nanocrystals with different concentrations of BPA and DBP followed by magnetic separation. The concentrations of BPA and DBP ranged from 5 to 30 ppm. The amount adsorbed was obtained as the difference in the concentrations of BPA and DBP in the solution, before addition of CMCD-Fe_3O_4@TiO_2 and after removal of the nanocrystals by magnetic separation, following equilibration. Concentrations of BPA and DBP were determined by liquid chromatography. The adsorption isotherms for both BPA and DBP follow the Langmuir isotherm (Figure 5), but the maximum uptake values differ. For BPA, the maximum uptake corresponds to a molar ratio of BPA to the anchored cyclodextrins of 0.87, while for DBP, the ratio is 0.72. This difference is probably a reflection of the fact that in aqueous solutions the association constant of the BPA-β-cyclodextrin complex (35×10^3 M^{-1})[34] has a higher value as compared to the DBP complex (1.1×10^3 M^{-1}).[35] The sorption isotherms highlight the importance of the anchored cyclodextrin cavities by not only ensuring that CMCD-Fe_3O_4@TiO_2 is water-dispersible but also providing hydrophobic pockets for the inclusion of the nonpolar BPA and DBP molecules.

Photocatalytic Degradation of Bisphenol A (BPA) and Dibutyl Phthalte (DBP). The degradation of BPA and DBP under illumination was carried out using a Hg vapor lamp in the presence of CMCD-Fe_3O_4@TiO_2. The concentrations of BPA and DBP were typically 20 ppm, and the weight of CMCD-Fe_3O_4@TiO_2 in the dispersion was 1 mg/mL. Aliquots were collected after regular intervals of illumination time, and the concentration of the organic EDCs in solution was estimated using liquid chromatography after removing the CMCD-Fe_3O_4@TiO_2 from the dispersion by magnetic separation. For comparison, blank experiments were performed using a stirred suspension of the bare Fe_3O_4@TiO_2. In the absence of anchored cyclodextrin cavities, the Fe_3O_4@TiO_2 nanoparticles are not water-dispersible.

The variation in the concentrations of BPA and DBP in the solution in the presence of CMCD-Fe_3O_4@TiO_2 and Fe_3O_4@TiO_2 as a function of illumination time is shown in Figure 6. It may be seen that degradation is more efficient in the CMCD-Fe_3O_4@TiO_2 dispersion as compared to the Fe_3O_4@TiO_2 suspension. In the presence of CMCD-Fe_3O_4@TiO_2, the photocatalytic degradation of BPA is complete within 60 min, whereas in the Fe_3O_4@TiO_2 suspensions, degradation is incomplete even after 180 min of illumination. Similar results are observed for the degradation of DBP. The effect of pH on the photocatalytic degradation efficiency was also investigated. It was found that the degradation of BPA by the CMCD-Fe_3O_4@TiO_2 was most efficient in the pH range of 7−9 and for DBP in the pH range of 7−10 (see Supporting Information).

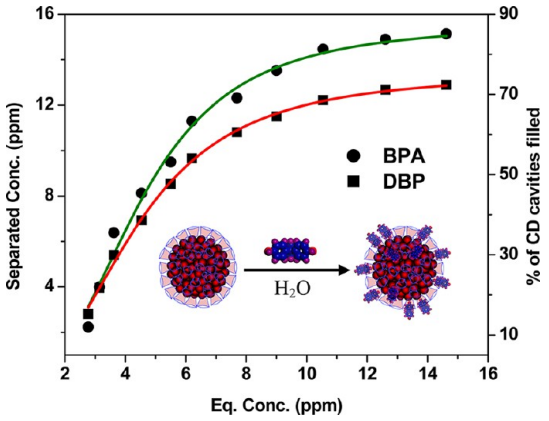

Figure 5. Sorption isotherms for the adsorption of bisphenol A and dibutyl phthalate by CMCD-Fe_3O_4@TiO_2 nanoparticles. The solid line is the fit to the Langmuir adsorption isotherm. The inset shows a schematic representation of the adsorption of bisphenol A by the CMCD-Fe_3O_4@TiO_2 nanoparticles.

The superior photocatalytic efficiency of CMCD-Fe_3O_4@TiO_2 for the degradation of BPA and DBP as compared to Fe_3O_4@TiO_2 is due to a combination of factors: its water dispersibility and the presence of the hydrophobic cyclodextrin cavities that can include the nonpolar organic molecules. It is reasonably well-established that it is the photogenerated conduction band electrons (e_{CB}^-) and valence band holes (h_{VB}^+) that are responsible for the photocatalytic activity of TiO_2.[7] When cyclodextrin cavities are anchored on the surface of TiO_2, the photogenerated holes (h_{VB}^+) can be trapped by the cyclodextrin cavities (h_{CD}^+). These holes (h_{CD}^+) mediate the one-electron oxidation process of organic molecules included within the cyclodextrin cavities.[36] In some cases, the holes in the valence band (h_{VB}^+) can directly oxidize the included molecules. In both cases, the included molecules are converted to radical cations that are subsequently excluded from the hydrophobic cyclodextrin cavities to undergo further transformations and rearrangements.[37] In the present study, it is the "capture" of the organic pollutants by the anchored cyclodextrin cavities that brings the organic EDCs and the TiO_2 shell in proximity, facilitating the initial oxidation step of the photodegradation reaction. The superior catalytic efficiency of the CMCD-Fe_3O_4@TiO_2 nanoparticles as compared to the bare Fe_3O_4@TiO_2 particles is a consequence of the inclusion of the EDC molecules within the anchored cyclodextrin cavities. The exclusion of the products of photodegradation ensures that the anchored cyclodextrin cavities of the CMCD-Fe_3O_4@TiO_2 nanoparticles are always available for the inclusion of the pollutant EDC molecule.

The intermediate products of the photocatalytic degradation of BPA and DBP by CMCD-Fe_3O_4@TiO_2

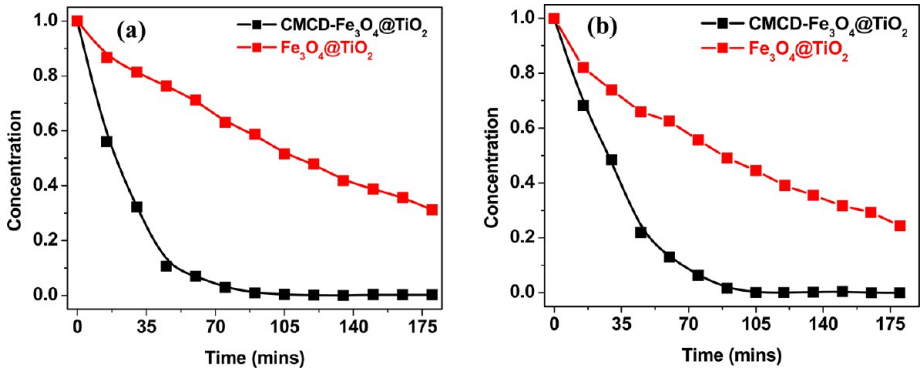

Figure 6. Photocatalytic degradation of (a) bisphenol A and (b) dibutyl phthalate in CMCD-Fe_3O_4@TiO_2 dispersions and Fe_3O_4@TiO_2 suspensions as a function of illumination time.

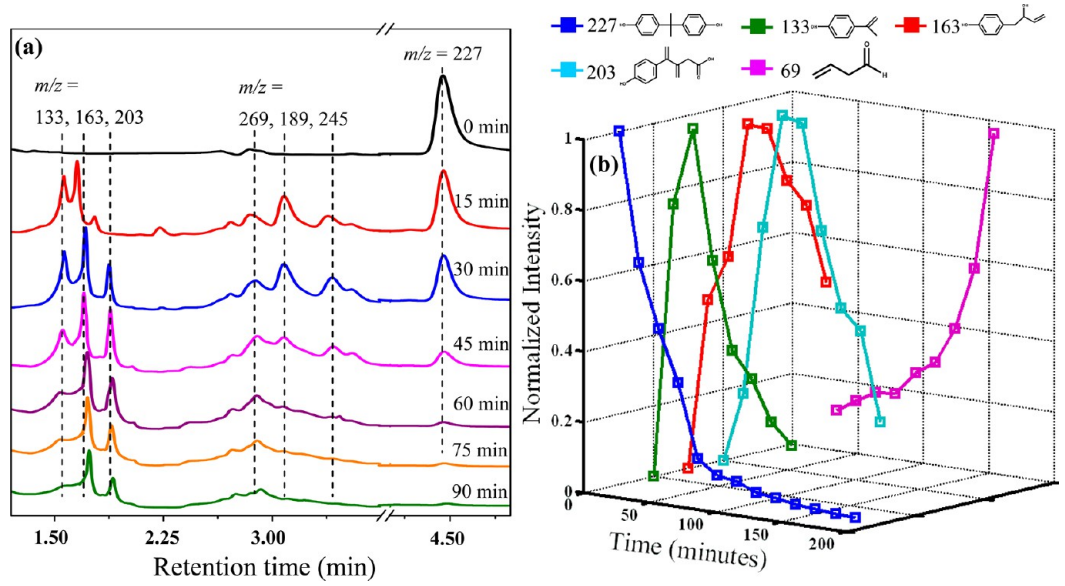

Figure 7. Photocatalytic degradation of bisphenol A by CMCD-Fe_3O_4@TiO_2. (a) LC-MS chromatograms for different UV irradiation times. The time in minutes is indicated. The *m/z* values of the ions corresponding to the species with different retention times are also indicated. (b) Evolution of the products of the photodegradation of BPA with irradiation time. The molecular species corresponding to the different *m/z* ions is shown.

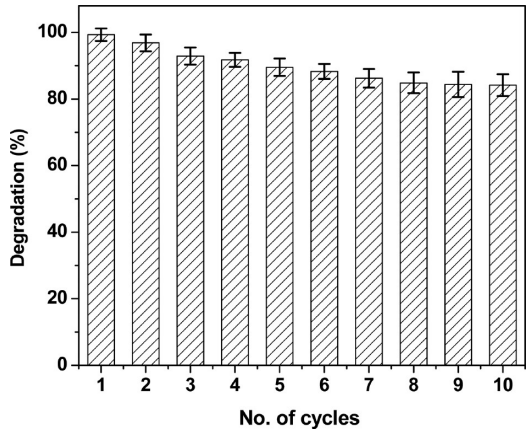

Figure 8. Variation in the efficiency of the CMCD-Fe_3O_4@TiO_2 for the photocatalytic degradation of bisphenol A with cycling. The exposure time in each cycle was 60 min.

for different periods of exposure to light was investigated by LC-MS-MS analysis using acetonitrile/water as the eluent. The chromatograms for the degradation of BPA for seven different UV exposure times are shown in Figure 7a. The products at different retention times were mass-analyzed in the negative ion mode, and their evolution with irradiation time is displayed in Figure 7b. The six main product ions seen in the degradation of BPA appearing at different retention times are *m/z* 133, 163, 203, 269, 189, and 245. The *m/z* 227 ion (retention time = 4.5 min) observed in the chromatograms at short exposure times is identified as the deprotonated BPA molecular ion. After 60 min of UV exposure, this ion is no longer observed in the chromatograms. Ions with molecular weights of *m/z* 245 and 269 observed in the chromatograms recorded after irradiation for 15 and 30 min suggest that the first step in the photocatalytic degradation is the reaction of hydroxyl radicals with the phenyl ring of bisphenol A. Similar mechanisms have been proposed in the literature.[19] At longer exposure times, the observed intermediates are mainly the aromatic ring-opening products. Results for the photodegradation of DBP show a similar trend and are described in the Supporting Information.

An important consideration for the application of the photocatalytic nanomaterials in water remediation is their separation and reusability. The photocatalytic efficiency of the CMCD-Fe_3O_4@TiO_2 nanoparticles for multiple usages was investigated. The CMCD-Fe_3O_4@TiO_2 nanoparticles that were magnetically separated from the dispersion after the photocatalytic degradation of BPA (Figure 6a) were reused for the photodegradation of a freshly prepared BPA solution. As in the experiments mentioned earlier, the BPA concentrations were determined by liquid chromatography and the UV exposure time was 60 min. The CMCD-Fe_3O_4@TiO_2 nanoparticles were again magnetically separated and the experiments repeated. The results of the photodegradation studies are shown in Figure 8. It may be seen that even after 10 cycles the efficiency of the CMCD-Fe_3O_4@TiO_2 for the photocatalytic degradation of BPA remains high, maintaining 90% efficiency as compared to the first use efficiency.

CONCLUSIONS

Heterogeneous photocatalytic degradation of harmful organic pollutants is a promising technique for wastewater treatment and water purification. Its inherent advantage includes complete mineralization and high degradation efficiency in treating most

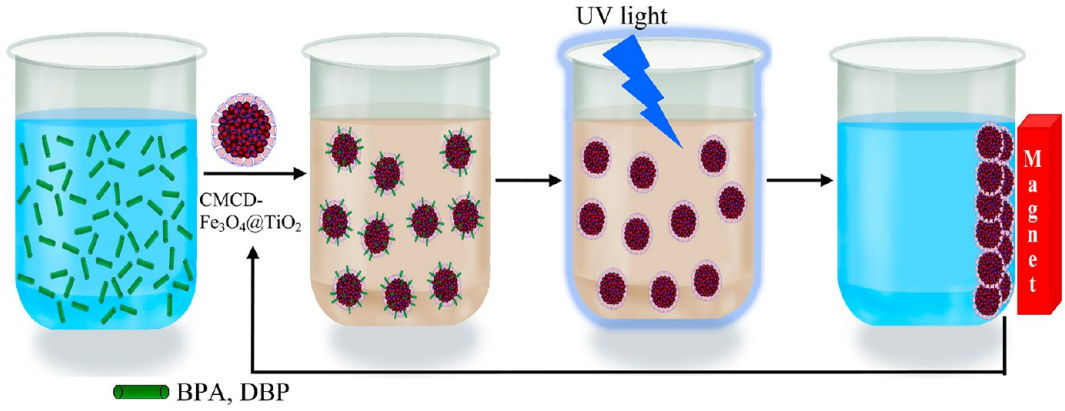

Scheme 3

organic compounds at low concentrations. Water-dispersible, photocatalytic Fe_3O_4@TiO_2 core–shell nanoparticles have been prepared by anchoring cyclodextrin cavities to the TiO_2 shell, and their ability to photodegrade endocrine-disrupting chemicals, bisphenol A and dibutyl phthalate, present in water, has been demonstrated. The particles, which are typically 12 nm in diameter, are magnetic and may be removed from the dispersion by magnetic separation and reused. The TiO_2 shell is the photocatalytically active element in the hybrid nanostructure and from X-ray diffraction and electron microscopy shown to be structurally amorphous. It crystallizes as the anatase phase on thermal annealing in the water-insoluble Fe_3O_4@TiO_2. The 9 nm crystalline Fe_3O_4 core is superparamagnetic at room temperature and exhibits a blocking temperature of 115 K. The cyclodextrin-functionalized Fe_3O_4@TiO_2 nanoparticles exhibit appreciable saturation magnetization values at room temperature (28 emu/g) which allows the particles to be removed from aqueous dispersions on application of modest magnetic fields (<0.4 T). The exposed hydroxyl groups of the cyclodextrin cavities, coordinatively linked to the TiO_2 shell *via* a carboxymethyl linkage, are responsible for the aqueous dispersibility of the particles. The anchored cyclodextrins also provide the hydrophobic cavities for the capture of the nonpolar organic pollutants, bisphenol A and dibutyl phthalate, present in water. β-Cyclodextrin is known to form 1:1 inclusion complexes with both bisphenol A and dibutyl phthalate. The inclusion of the bisphenol A and dibutyl phthalate in the anchored cyclodextrin is crucial for it allows the organic molecules to come in close proximity to the surface of the TiO_2 shell and makes the photodegradation efficiencies far superior to that of the bare Fe_3O_4@TiO_2 nanoparticles. Once the photodegradation is complete, the cyclodextrin-functionalized Fe_3O_4@TiO_2 nanoparticles may be removed from the dispersion and reused. The entire sequence from the capture to the photodestruction of the endocrine-disrupting chemical, bisphenol A and dibutyl phthalate, is summarized pictorially in Scheme 3.

Although the scope of the present study is limited to a laboratory demonstration of the capture and photodegradation of endocrine-disrupting chemicals, we believe that the cyclodextrin-functionalized Fe_3O_4@TiO_2 can provide an efficient, environmentally benign, and low-cost approach for the removal and photodegradation of recalcitrant organic compounds present in water supplies. An attractive feature of these nanomaterials is that they may be completely removed from the dispersion and reused with little or no loss of catalytic activity.

EXPERIMENTAL SECTION

Materials. Tetrabutyl titanate (Sigma-Aldrich), dibutyl phthalate (Alfa-Aesar), acetylacetone, ethanol, cyanamide, bisphenol A (SD Fine Chemicals), and β-cyclodextrin (Hi-media Laboratories) were used as received without further purification.

Preparation of β-Cyclodextrin-Functionalized Fe_3O_4@TiO_2. Water-dispersible cyclodextrin-capped Fe_3O_4@TiO_2 nanoparticles were prepared by a two-step procedure. In the first step, monodisperse Fe_3O_4@TiO_2 core–shell nanocrystals were prepared. The procedure required water-dispersible Fe_3O_4 nanocrystals which were then coated with a TiO_2 shell. Spherical iron oxide nanoparticles were first prepared, heating a mixture of 0.267 g of FeOOH fine powder, oleic acid (4.73 mL), and 1-octadecene (8.0 mL) at 310 °C for 30 min under nitrogen mixture with constant stirring. This procedure is known to give monodisperse oleate-capped spherical iron oxide nanocrystals. The Fe_3O_4 was rendered water-dispersible by capping with cyclodextrin cavities by a simple mass exchange reaction on addition of carboxymethyl–β-cyclodextrin (CMCD) to the oleate-capped Fe_3O_4 nanocrystals following an earlier reported procedure. It may be mentioned that at this stage the role of the cyclodextrin cavities is limited to rendering the Fe_3O_4 nanocrystals water-dispersible; they are stripped off the surface on formation of the TiO_2 shell. For forming the shell, 50 mg of the water-dispersible Fe_3O_4 nanoparticles was added to 5 mL of water and sonicated for 10 min followed by addition of 90 mL of ethanol. A separate solution containing 10 mL of ethanol, 1 mL of acetylacetone, and 0.75 mL of tetrabutyl titanate (TBT) was added dropwise to the Fe_3O_4 solution, sonicated, and then refluxed at 90 °C for 90 min. The core–shell Fe_3O_4@TiO_2 nanoparticles were removed by magnetic separation and washed with ethanol and redispersed in 5 mL of water, and the pH of the solution was adjusted to 6 using a phosphate

buffer. To this dispersion were added 100 mg of carboxymethyl−β-cyclodextrin (CMCD) along with 100 μL of cyanamide (50% aqueous solution) and refluxed in an oil bath at 90 °C for 4 h. CMCD-Fe_3O_4@TiO_2 nanoparticles were washed with water following magnetic separation.

Synthesis of Carboxymethyl−β-Cyclodextrin. The carboxymethyl−β-cyclodextrin (CMCD) was prepared by treating a mixture of β-cylcodextrin (3 g, 18.6 mmol) in 3 mL of water and sodium hydroxide (2.79 g) in water (10 mL) with 8.1 mL of 16.3% monochloroacetic acid solution at 50 °C for 4 h. The pH of the reaction mixture was adjusted to 4 by adding HCl. The product, CMCD, was precipitated by addition of methanol and acetone.

Physical Characterization. Powder X-ray diffraction patterns were recorded on a Bruker D8-Advance diffractometer using Cu Kα radiation of λ = 1.54 Å. Data were collected at a scan rate of 0.017°/s. High-resolution transmission electron microscopy (HRTEM) and bright-field images were recorded on a JEOL JEM-2100F, fitted with bottom-mounted Olympus Keen View G2 CCD camera and an Oxford INCA energy EDAX attachment. Dark-field STEM images were recorded on ADF detector with the collection angle varying from 55 to 148 mrad. Analysis of the HRTEM images was done using the Olympus-SIS iTEM software package. Magnetic properties were measured using a Quantum Design MPMS XL-5 superconducting quantum interference device (SQUID) magnetometer. FTIR spectra were recorded on a Perkin-Elmer Spectrum One machine operating at 4 cm^{-1} resolution. UV−vis spectra were recorded on a Perkin-Elmer Lambda35 spectrometer. Elemental analysis was done using a Thermo Scientific Flash 2000 elemental analyzer. Liquid chromatography (LC) analysis was done using a Thermo LCQ Deca XP MAX spectrometer fitted with electrospray ionization (ESI) source for mass analysis. The mass spectrometer was operated in the m/z 50−350 range in the negative ion mode (for DBP the positive ion mode was used). The temperature of the heated capillary was 350 °C. The source and cone voltages were set to 5000 and 40 V, respectively.

Adsorption Measurements. Adsorption measurements were recorded in the batch mode. A weighed quantity (typically 15 mg) of the CMCD-Fe_3O_4@TiO_2 was dispersed in aqueous solution (15 mL) of differing concentrations of bisphenol A (BPA) and dibutyl phthalate (DBP). The concentration of BPA and DBP ranged from 5 to 30 ppm. The dispersions were allowed to equilibrate for 24 h and the CMCD-Fe_3O_4@TiO_2 nanocrystals separated by application of a magnetic field using a small permanent magnet (0.4 T). The nanocrystals separated from the solution within 2 to 3 min. The concentration of BPA and DBP in the residual solution was estimated as the area of the peak obtained in the liquid chromatogram. The LC was equipped with a UV detector and a C18 column (4.6 mm × 250 mm, 5 μm). BPA and DBP were detected by monitoring the elution at 275 nm. The eluent was a mixture of acetonitrile/water (50/50, v/v) at a flow rate of 1.0 mL min^{-1}. The injected volume was 20 μL.

Photodegradation Studies. Photodegradation studies were done by irradiating dispersions with a mercury vapor lamp (400 W; 17 mW/cm^2). Fifteen milliliters of the solution containing either BPA (20 ppm) or DBP (20 ppm) was stirred with 15 mg of CMCD-Fe_3O_4@TiO_2 and equilibrated prior to irradiation. Aliquots were drawn after differing intervals of irradiation time, and the CMCD-Fe_3O_4@TiO_2 was separated from the dispersion with a magnet. The concentration of BPA (or DBP) was estimated by using LC-MS. The products were identified using the LC-MS/MS technique. The mobile phase was a mixture of acetonitrile/water (50/50, v/v) at a flow rate of 1.0 mL min^{-1}.

Conflict of Interest: The authors declare no competing financial interest.

Acknowledgment. The authors acknowledge support of the Indian Institute of Science in setting up the Chemical Sciences Division TEM facility, and the help of Mr. Amit Gupta in recording TEM images.

Supporting Information Available: (S1) TGA of Fe_3O_4@TiO_2 and CMCD-Fe_3O_4@TiO_2 nanoparticles. (S2) Elemental analysis of CMCD and CMCD-Fe_3O_4@TiO_2 nanoparticles. (S3) Core level X-ray photoelectron spectroscopy of the CMCD-Fe_3O_4@TiO_2 nanoparticles. (S4) Infrared spectral assignments of CMCD and CMCD-Fe_3O_4@TiO_2 nanoparticles. (S5) Summary of the Rietveld refinement results for the thermally annealed Fe_3O_4@TiO_2 nanocrystals. (S6) Atomic positions in the thermally annealed Fe_3O_4@TiO_2 nanocrystals as obtained from a Rietveld analysis of the X-ray diffraction patterns. (S7) Efeect of pH on the photocatalytic degradation of BPA and DBP. (S8) Mass spectral analysis of BPA and intermediates of the photocatalytic degradation. (S9) Photocatalytic degradation of DBP by CMCD-Fe_3O_4@TiO_2 nanoparticles. (S10) Mass spectral analysis of DBP and intermediates of the photocatalytic degradation. This material is available free of charge *via* the Internet at http://pubs.acs.org.

REFERENCES AND NOTES

1. Rajeshwar, K. Solar Energy Conversion and Environmental Remediation Using Inorganic Semiconductor−Liquid Interfaces: The Road Traveled and the Way Forward. *J. Phys. Chem. Lett.* **2011**, *2*, 1301–1309.
2. O'Shea, K. E.; Dionysiou, D. D. Advanced Oxidation Processes for Water Treatment. *J. Phys. Chem. Lett.* **2012**, *3*, 2112–2113.
3. Lee, J.; Kim, J.; Choi, W. TiO_2 Photocatalysis for the Redox Conversion of Aquatic Pollutants. *ACS Symp. Ser.* **2011**, *1071*, 199–222.
4. Legrini, O.; Oliveros, E.; Braun, A. M. Photochemical Processes for Water Treatment. *Chem. Rev.* **1993**, *93*, 671–698.
5. Linsebigler, A. L.; Lu, G.; Yates, J. T. Photocatalysis on TiO_2 Surfaces: Principles, Mechanisms, and Selected Results. *Chem. Rev.* **1995**, *95*, 735–758.
6. Serpone, N.; Emeline, A. V. Semiconductor Photocatalysis—Past, Present, and Future Outlook. *J. Phys. Chem. Lett.* **2012**, *3*, 673–677.
7. Hoffmann, M. R.; Martin, S. T.; Choi, W.; Bahnemann, B. W. Environmental Applications of Semiconductor Photocatalysis. *Chem. Rev.* **1995**, *95*, 69–96.
8. Ma, W.-F.; Zhang, Y.; Li, L.-L.; You, L.-J.; Zhang, P.; Zhang, Y.-T.; Li, J.-M.; Yu, M.; Guo, J.; Lu, H.-J.; *et al.* Tailor-Made Magnetic Fe_3O_4@mTiO_2 Microspheres with a Tunable Mesoporous Anatase Shell for Highly Selective and Effective Enrichment of Phosphopeptides. *ACS Nano* **2012**, *6*, 3179–3188.
9. Li, Y.; Wu, J.; Qi, D.; Xu, X.; Deng, C.; Yanga, P.; Zhang, X. Novel Approach for the Synthesis of Fe_3O_4@TiO_2 Core−Shell Microspheres and Their Application to the Highly Specific Capture of Phosphopeptides for MALDI-TOF MS Analysis. *Chem. Commun.* **2008**, 564–566.
10. Xuan, S.; Jiang, W.; Gong, X.; Hu, Y.; Chen, Z. Magnetically Separable Fe_3O_4/TiO_2 Hollow Spheres: Fabrication and Photocatalytic Activity. *J. Phys. Chem. C* **2009**, *113*, 553–558.
11. Liu, Z.; Bai, H.; Sun, D. D. Facile Fabrication of Porous Chitosan/TiO_2/Fe_3O_4 Microspheres with Multifunction for Water Purifications. *New J. Chem.* **2011**, *35*, 137–140.
12. Yavuz, C. T.; Mayo, J. T.; Yu, W. W.; Prakash, A.; Falkner, J. C.; Yean, S.; Cong, L.; Shipley, H. J.; Kan, A.; Tomson, M.; *et al.* Low-Field Magnetic Separation of Monodisperse Fe_3O_4 Nanocrystals. *Science* **2006**, *314*, 964–967.
13. Chalasani, R.; Vasudevan, S. Cyclodextrin Functionalized Magnetic Iron Oxide Nanocrystals: A Host-Carrier for Magnetic Separation of Non-polar Molecules and Arsenic from Aqueous Media. *J. Mater. Chem.* **2012**, *22*, 14925–14931.
14. Auriol, M.; Filali-Meknassi, Y.; Tyagi, R. D.; Adams, C. D.; Surampalli, R. Y. Endocrine Disrupting Compounds Removal from Wastewater, a New Challenge. *Process Biochem.* **2006**, *41*, 525–539.
15. Staples, C. A.; Dom, P. B.; Klecka, G. M.; O'Block, S. T. A Review of the Environmental Fate, Effects, and Exposures of Bisphenol A. *Chemosphere* **1998**, *36*, 2149–2173.
16. Julinová, M.; Slavík, R. Removal of Phthalates from Aqueous Solution by Different Adsorbents: A Short Review. *J. Environ. Manag.* **2012**, *94*, 13–24.
17. Sin, J.-C.; Lam, S.-M.; Mohamed, A. R.; Lee, K.-T. Degrading Endocrine Disrupting Chemicals from Wastewater by

TiO_2 Photocatalysis: A Review. *Int. J. Photoenergy* **2012**, *2012*, 1–23.
18. Ohko, Y.; Ando, I.; Niwa, C.; Tatsuma, T.; Yamamura, T.; Nakashima, T.; Kubota, Y.; Fujishima, A. Degradation of Bisphenol A in Water by TiO_2 Photocatalyst. *Environ. Sci. Technol.* **2001**, *35*, 2365–2368.
19. Guo, C.; Ge, M.; Liu, L.; Gao, G.; Feng, Y.; Wang, Y. Directed Synthesis of Mesoporous TiO_2 Microspheres: Catalysts and Their Photocatalysis for Bisphenol A Degradation. *Environ. Sci. Technol.* **2010**, *44*, 419–425.
20. Kaneco, S.; Katsumata, H.; Suzuki, T.; Ohta, K. Titanium Dioxide Mediated Photocatalytic Degradation of Dibutyl Phthalate in Aqueous Solution-Kinetics, Mineralization and Reaction Mechanism. *Chem. Eng. J.* **2006**, *125*, 59–66.
21. Chalasani, R.; Vasudevan, S. Form, Content, and Magnetism in Iron Oxide Nanocrystals. *J. Phys. Chem. C* **2011**, *115*, 18088–18093.
22. Pastoriza-Santos, I.; Koktysh, D. S.; Mamedov, A. A.; Giersig, M.; Kotov, N. A.; Liz-Marzán, L. M. One-Pot Synthesis of Ag@TiO_2 Core−Shell Nanoparticles and Their Layer-by-Layer Assembly. *Langmuir* **2000**, *16*, 2731–2735.
23. Chen, H.-J.; Wang, L.; Chiu, W.-Y. Chelation and Solvent Effect on the Preparation of Titania Colloids. *Mater. Chem. Phys.* **2007**, *101*, 12–19.
24. Badruddoza, A. Z. M.; Tay, A. S. H.; Tan, P. Y.; Hidajat, K.; Uddin, M. S. Carboxymethyl−β-Cyclodextrin Conjugated Magnetic Nanoparticles as Nano-adsorbents for Removal of Copper Ions: Synthesis and Adsorption Studies. *J. Hazard. Mater.* **2011**, *185*, 1177–1186.
25. Czanderna, A. W.; Rao, C. N. R.; Honig, J. M. The Anatase-Rutile Transition. Part 1—Kinetics of the Transformation of Pure Anatase. *Trans. Faraday Soc.* **1958**, *54*, 1069–1073.
26. Reyes-Coronado, D.; Rodríguez-Gattorno, G.; Espinosa-Pesqueira, M. E.; Cab, C.; Coss, R. D.; Oskam, G. Phase-Pure TiO_2 Nanoparticles: Anatase, Brookite and Rutile. *Nanotechnology* **2008**, *19*, 145605-1–145605-10.
27. Lee, J. S.; You, K. W.; Park, C. B. Highly Photoactive, Low Bandgap TiO_2 Nanoparticles Wrapped by Graphene. *Adv. Mater.* **2012**, *24*, 1084–1088.
28. Hunter, R. J. Foundations of Colloid Science. In *Electrokinetics and the Zeta Potential*; Oxford University Press: New York, 2001; Vol. 2, pp 376−377.
29. Rodriguez-Carvajal, J. *FullProf SUITE*; LLB Saclay & LCSIM: Rennes, France, 2003.
30. Makhlouf, S. A.; Parker, F. T. Magnetic Hysteresis Anomalies in Ferritin. *Phys. Rev. B* **1997**, *55*, R14717–R14720.
31. Martínez-Boubeta, C.; Simeonidis, K.; Angelakeris, M.; Pazos-Pérez, N.; Giersig, M.; Delimitis, A.; Nalbandian, L.; Alexandrakis, V.; Niarchos, D. Critical Radius for Exchange Bias in Naturally Oxidized Fe Nanoparticles. *Phys. Rev. B* **2006**, *74*, 054430-1–054430-10.
32. Nogués, J.; Schuller, I. K. Exchange Bias. *J. Magn. Magn. Mater.* **1999**, *192*, 203–232.
33. Skumryev, V.; Stoyanov, S.; Zhang, Y.; Hadjipanayis, G.; Givord, D.; Nogués, J. Beating the Superparamagnetic Limit with Exchange Bias. *Nature* **2003**, *423*, 850–853.
34. Kitano, H.; Endo, H.; Gemmei-Ide, M.; Kyogoku, M. Inclusion of Bisphenols by Cyclodextrin Derivatives. *J. Inclusion Phenom. Macrocyclic Chem.* **2003**, *47*, 83–90.
35. Murai, S.; Imajo, S.; Takasu, Y.; Takahashi, K.; Hattori, K. Removal of Phthalic Acid Esters from Aqueous Solution by Inclusion and Adsorption on β-Cyclodextrin. *Environ. Sci. Technol.* **1998**, *32*, 782–787.
36. Tachikawa, T.; Tojo, S.; Fujitsuka, M.; Majima, T. One-Electron Oxidation Pathways during β-Cyclodextrin-Modified TiO_2 Photocatalytic Reactions. *Chem.—Eur. J.* **2006**, *12*, 7585–7594.
37. Tachikawa, T.; Tojo, S.; Fujitsuka, M.; Majima, T. Exclusion of Aromatic Radical Cations from Cyclodextrin Nanocavity Studied by Pulse Radiolysis. *J. Phys. Chem. B* **2005**, *109*, 17460–17466.